RESEARCH ARTICLE | FEBRUARY 11 2022

Magnetic transition behavior in epitaxial $Fe_{47}Rh_{47}Pd_6$ films

Hideo Sato; Neha Pachauri; Sahar Keshavarz; Chhatra R. Joshi; Hwachol Lee; Gary J. Mankey ;
Patrick LeClair

Journal of Vacuum Science & Technology A 40, 023406 (2022)
https://doi.org/10.1116/6.0001573

JVST A
Journal of Vacuum Science & Technology A
ARTICLE
avs.scitation.org/journal/jva

Magnetic transition behavior in epitaxial $Fe_{47}Rh_{47}Pd_6$ films

Cite as: J. Vac. Sci. Technol. A **40**, 023406 (2022); doi: 10.1116/6.0001573
Submitted: 20 October 2021 · Accepted: 27 December 2021 ·
Published Online: 11 February 2022

Hideo Sato, Neha Pachauri, Sahar Keshavarz, Chhatra R. Joshi, Hwachol Lee, Gary J. Mankey,[a] and Patrick LeClair

AFFILIATIONS

Department of Physics and Astronomy, The University of Alabama, Tuscaloosa, Alabama 35487

[a]**Electronic mail:** gmankey@ua.edu

ABSTRACT

The properties of Fe–Rh–Pd epitaxial thin films grown on MgO(001) were studied as a function of growth temperature. Films grown above 400 °C exhibit a first-order antiferromagnetic to ferromagnetic magnetic phase transition with a transition temperature that decreases as the growth temperature is increased. The chemical order parameter computed from the ratio of intensities of the (001) and (002) diffraction peaks is nearly independent of the growth temperature, while the lattice constants change slightly. A comparison of our structural, magnetic, and electrical transport results with first-principle-based calculations as well as literature results indicates that the transition temperature of Fe–Rh-based alloy films depends sensitively on the lattice parameters and is of electronic origin. The transition temperature and its width can be tuned over a wide range by controlling the crystal structure via growth conditions or postdeposition annealing.

I. INTRODUCTION

The Fe–Rh system has attracted much interest due to its wide range of magnetic properties. It exhibits a first-order magnetic transition around 400 K from antiferromagnetic[1,2] to ferromagnetic as the sample is heated. This transition temperature can be tuned by adding a third element to the compound. For example, the addition of Ni and Pd decreases the transition temperature, whereas the addition of Pt and Ir increases it.[3–6] The transition temperature in FeRh-based thin films can also be tuned by changing the growth conditions,[7,8] which suggests the sensitivity of the magnetic transition to structural parameters and chemical order. Since FeRh-based alloys have a transition from ferromagnetism to antiferromagnetism near room temperature; they may have potential technological applications in, e.g., heat assisted magnetic recording,[9–11] magnetoresistive sensing,[3,12] magnetic refrigeration,[13,14] etc. In this work, films with a reduced transition temperature below room temperature are studied to isolate the factors that determine the nature of the phase transition.

For these potential applications to become reality, a fuller understanding of the seemingly subtle factors that have a profound effect on the phase transition and its properties (for example, its rapidity[15]) is necessary, particularly, in well-characterized thin films. Several studies have focused on relatively thick films with postdeposition annealing treatments at high temperature (up to 800 °C)[16] or bulk samples.[3–5] Investigations of films in the range of 100 nm and below is required to gauge their potential for applications. For example, a study of a nominal 50 nm film of FeRh with 3% Pd doping showed that there is a coexistence of ferromagnetism and antiferromagnetism near the phase transition.[17] For 100 nm thick films of pure FeRh, the phase transition temperature can be altered by 10% with different capping layers[18] deposited to prevent oxidation. This dramatic change emphasizes the importance of properly characterizing the crystal structure and morphology of thinner layers.

Generally, larger and more uniform strain can be induced in thinner films, which can yield distinctly different magnetic properties owing to the modification of the exchange interactions as interatomic distances are altered. From a fundamental point of view, it is, therefore, also of interest to study the magnetic properties of Fe–Rh and Fe–Rh–M films with thicknesses in the range where significant strain can be induced, allowing an investigation of the roles of the competing exchange interactions in affecting the magnetic phase transition.

The exchange energy can be a sensitive function of interatomic spacing, changing from antiferromagnetic to ferromagnetic as the lattice is expanded. The introduction of dopant atoms is one mechanism by which interatomic spacing may be readily altered, altering the exchange energy and either increasing (e.g., Pt and Ir) or decreasing (e.g., Ni and Pd) the temperature of the AF–F phase transition.[3–5] The overall trend in the shift of the phase transition temperature follows from a simple argument based on examining the differences in covalent radii.[19] For Pd dopants (0.139 nm), the covalent radius is larger than that of Rh (0.135 nm). This difference should result in an increase of the interatomic spacing and, therefore, a net reduction in the exchange energy, yielding a lower transition temperature. For Pt (0.128 nm) dopants with a smaller covalent radius than Rh, the lattice should be contracted, and the resulting increase in the exchange energy yields an increase of the phase transition temperature. This simple argument works for Pd and Pt dopants but breaks down when Ni (0.124 nm) and Ir (0.141 nm) are considered.[4] The reason for this difficulty is that the moments on the dopant atoms are not considered nor are higher order exchange interactions mediated by the dopant atoms. For alloys with equal Fe and Rh concentration, dopant atoms may substitute either of the base alloy atoms as illustrated in Fig. 1, and reducing the Fe concentration may further depress the transition temperature.

In this study, the degree of *structural* order is shown to significantly influence the magnetic and structural properties of 30 nm thick Fe–Rh–Pd films, even while the *chemical* order parameter remains essentially constant. A comparison of our results with first-principles-based calculations and existing literature points toward the importance of the competing exchange interactions in Fe–Rh-based alloys and their sensitive dependence on lattice parameters, with an ultimately electronic origin of the phase transition.

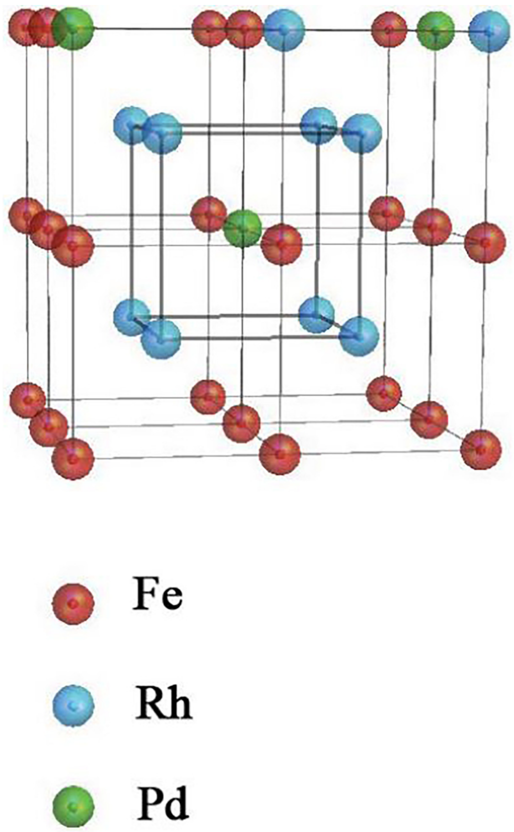

FIG. 1. Model B2 structure for Fe–Rh–Pd films. Pd randomly substitutes on both Fe and Rh sites. The B2 structure is two interpenetrating simple cubic lattices with the basis of (0, 0, 0) for type 1 atoms and ($a/2$, $a/2$, $c/2$) for type 2 atoms, with $a = c$. The c-axis is vertical in the figure.

II. EXPERIMENTAL DETAILS

All Fe–Rh–Pd films were fabricated in an ultrahigh vacuum magnetron sputtering system with a background pressure of less than 9×10^{-7} Pa. Films of Fe–Rh–Pd were directly deposited on MgO(001) substrates using a target of nominal composition $Fe_{47}Rh_{47}Pd_6$. Henceforth, we refer to the films as FePtRh for simplicity. All films were nominally 30 nm thick and were capped with a 2 nm thick Pt layer at room temperature in order to prevent oxidization. The growth temperature T_g was varied from 400 to 700 °C. The epitaxy and crystalline quality of our samples were ascertained using a Philips X'Pert x-ray diffraction (XRD) system, while the magnetic properties were evaluated using a Quantum Design magnetic properties measurement system (MPMS). Electrical properties were determined with standard four-point probe techniques using a Quantum Design physical properties measurement system (PPMS).

III. EXPERIMENTAL RESULTS

Figure 2 shows Cu K_α ($\lambda = 0.154$ nm) x-ray diffraction (XRD) θ–2θ scans for 30 nm FeRhPd films grown at growth temperatures T_g from 400 to 700 °C. All films showed only [002] planes oriented normal to the film plane, and FeRhPd [001] superstructure diffraction peaks can be clearly observed in all films, indicating that the ordered B2 (CsCl, Pm$\bar{3}$m) phase is present (though with a slight tetragonal distortion for lower T_g samples, see below). The ratio of integrated intensities of the superlattice (001) to fundamental (002) diffraction peaks is essentially constant, indicating little change in chemical order with varying growth temperature. However, the full-width at half-maximum (FWHM) for the (001) and (002) diffraction peaks, shown in Fig. 3, steadily decrease as growth temperature increases, indicating a steady improvement in the crystalline quality. The epitaxial growth of the Fe–Rh–Pd layers on MgO(001) substrates was confirmed by measuring FePtRh (101) and MgO (202) as a function of φ, shown in Fig. 4 for a sample with $T_g = 500$ °C. The φ scan results indicate fourfold in-plane symmetry, with the Fe–Rh–Pd[100] axis rotated by 45° with respect to the MgO[100] axis, as is frequently observed in cubic films deposited on MgO(001) substrates. The FWHM of the (101) peak ascertained from the φ scan is also shown in Fig. 3, showing a trend similar to the (001) and (002) peaks.

Since the magnetic transition of this material can only be observed in the B2-like (ordered) phase, it is necessary to evaluate the long-range chemical order parameter S in these films to quantify the degree to which B2 order is present throughout the films. (The tetragonal distortion observed is sufficiently small, <1%, as not to significantly affect the subsequent order parameter calculations, discussed further below.) The order parameter S can be

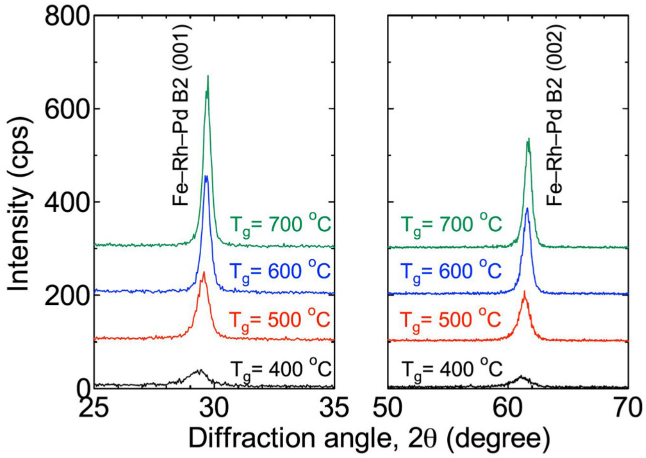

FIG. 2. X-ray diffraction near the (001) and (002) peaks for FeRhPd films deposited on MgO(001) substrates with increasing growth temperature. Curves are vertically offset for clarity.

determined from the integrated intensity ratios of the fundamental (200) and superlattice (100) reflections, provided one accounts for the appropriate structure factors and film thickness and Debye–Waller corrections.[1,3,20–22] The integrated intensity I of a given x-ray diffraction peak can, in general, be written as[20,22–24]

$$I = |F|^2 \Lambda G_t, \tag{1}$$

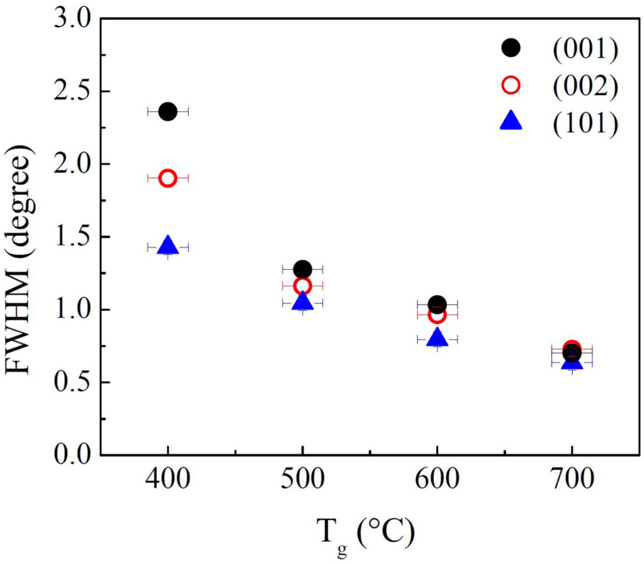

FIG. 3. Full-width at half-maximum of the FeRhPd (001) and (002) peaks vs growth temperature, indicating that crystalline quality increases for higher growth temperatures.

where $|F|^2$ is the square of the structure factor, Λ is the Lorentz polarization factor, and G_t is the film thickness correction factor. The Lorentz polarization factor for a single crystal in an unpolarized primary beam with incident angle θ and scattering angle 2θ is[20] $\Lambda = (1 + \cos^2 2\theta)/2 \sin 2\theta$. The thickness correction factor for a film of thickness t is given by[25] $G_t = 1 - \exp(-2\mu t/\sin\theta)$, where μ is the linear absorption coefficient. Considering first an Fe_xRh_{1-x} alloy in the B2 structure, the fundamental (200) structure factor is[23,24]

$$F_f = \frac{x}{1-x} f_{\text{tot, Fe}} + f_{\text{tot, Rh}}, \tag{2}$$

where $f_{\text{tot, Fe(Rh)}}$ is the total atomic scattering factor, x is the concentration of Fe, and $1 - x$ is the concentration of Rh. The superlattice (100) structure factor is[23,24]

$$F_s = \frac{x}{1-x} f_{\text{tot, Fe}} - f_{\text{tot, Rh}}. \tag{3}$$

The atomic scattering factors, accounting for dispersion and the Debye–Waller temperature corrections, can be written as[20,22–24,26]

$$f_{\text{tot}} = (f_o + f' + i f'')e^{-M}, \tag{4}$$

where f_o is the atomic scattering factor; f' and f'' are the real and imaginary dispersion corrections, respectively; and e^{-M} is the Debye–Waller correction.[20,22] All three scattering terms depend on the value of $\sin\theta/\lambda$ for given radiation of wavelength λ and incident angle θ. The exponent of the Deybe–Waller correction term takes the form $M = B \sin^2(\theta)/\lambda^2$, where B is the (temperature-dependent) Debye–Waller factor for each element.[20,24]

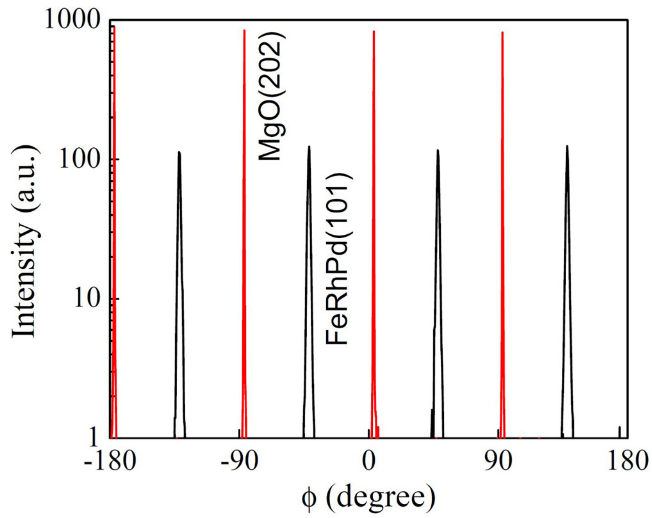

FIG. 4. φ scan of the MgO (202) and FeRhPd (101) peaks for a sample with $T_g = 500\,°C$, indicating that the Fe–Rh–Pd[100] axis is rotated by 45° with respect to the MgO [100] axis.

Of course, these structure factors above are correct only for an Fe_xRh_{1-x} alloy in which there is no site disorder. Since we have an alloy which is slightly Fe-deficient compared to the equiatomic alloy, site disorder must be present as a result. Still considering an Fe_xRh_{1-x} alloy, if there is a fraction y of Rh atoms on Fe sites due to an Fe deficiency, we may correct the structure factors following Xiao and Baker[23] as

$$F_f = \left[\frac{x(1+y)}{1-x}\right] f_{\text{tot, Fe}} + (1+y) f_{\text{tot, Rh}}, \tag{5}$$

$$F_s = \left[\frac{x(1+y)}{1-x}\right] f_{\text{tot, Fe}} - (1-y) f_{\text{tot, Rh}}. \tag{6}$$

In the present case, we have a nominal composition of $Fe_{47}Rh_{47}Pd_6$. In this case, there is a 3% excess of Rh+Pd compared to the parent $Fe_{50}Rh_{50}$ alloy. For that reason, we use $Y = 0.03$ to represent the ideal $Fe_{47}Rh_{47}Pd_6$ system because even for perfect ordering at this composition, there must be at least 3% of Rh+Pd atoms that occupy Fe sites.[23,24] Using these structure factors and the film thickness and Lorentz polarization factors above, one may calculate the superlattice I_s and fundamental I_f integrated intensities. The long-range order parameter S can then be determined from the experimentally observed integrated intensities via[20,23,24,26]

$$S^2 = \frac{(I_s/I_f)_{\text{obs}}}{(I_s/I_f)_{\text{calc}}}. \tag{7}$$

For Fe, we used the scattering factor terms f_o, f', f'' for the appropriate values of $\sin(\theta)/\lambda$[20] interpolated from the tables in Ref. 20 and the Deybe–Waller factors given in Refs. 26 and 27. Since the scattering factors for Rh and Pd are very similar,[20,28,29] and the Pd content is small, we have used the structure factor for an ideal Fe_xRh_{1-x} alloy with $1 - x = 0.53$ as the *combined* Rh+Pd concentration but replaced the individual Rh scattering factor terms with composition-weighted averages of those of Rh and Pd.[20,21] Similarly, we used a composition-weighted average for the Debye–Waller factors.[27,30] The linear absorption coefficient is a composition-weighted average of those for Fe, Rh, and Pd.[28,29] The resulting parameters for our calculation of the fully ordered $Fe_{47}Rh_{47}Pd_6$ superlattice (001) and fundamental (002) integrated diffraction intensities are shown in Table I.

TABLE I. Parameters used to calculate the (001) and (002) peak intensities for $Fe_{47}Rh_{47}Pd_6$ (see text for definitions). The Debye–Waller factor B is valid at 300 K, all quantities are taken for Cu K_α radiation (λ = 1.54 Å, E = 8.04 keV). The film thickness is t = 30 nm.

Atom	Peak	θ	B (Å^2)	μ (cm^{-1})	f_o	f'	f''
Fe	(001)	14.8	0.343	2424	21.36	−1.1	3.3
	(002)	30.8	0.343	2424	15.90	−1.1	3.3
Rh	(001)	14.8	0.153	2408	38.00	−0.5	4.0
	(002)	30.8	0.153	2408	29.71	−0.5	3.8
Pd	(001)	14.8	0.448	2476	38.90	−0.5	4.3
	(002)	30.8	0.448	2476	30.47	−0.5	4.1

Table II gives the measured I_s/I_f intensity ratio and calculated order parameter S as a function of T_g, confirming that S is almost independent of the growth temperature with an average value of $S \approx 0.95 \pm 0.05$. This indicates that the growth temperature had no significant influence on the degree of *chemical* ordering in this growth temperature range. This is in sharp contrast to our earlier work for $Fe_{25}Pt_{75}$ thin films, where changing the growth temperature in this range resulted in a large change in the order parameter.[26] On the other hand, the reduction of the FWHM of the (001) and (002) out-of-plane diffraction peaks as T_g increases indicates that crystalline quality is affected by growth temperature, and we find that the lattice constants also change as the growth temperature is increased, as shown in Fig. 5. For comparison, we have also prepared samples with $T_g = 400\,^\circ$C, which were subsequently annealed in vacuum to $T_a = \{500, 600, 700\}\,^\circ$C for 30 min, also shown in Table II. In all three cases, the order parameter and integral peak intensity ratios are identical within the uncertainty in the measurements.

In order to obtain accurate lattice constant values for our Fe–Rh–Pd films from the x-ray diffraction results, Cohen's method was used.[31,32] Although bulk Fe–Rh–Pd has the cubic B2 structure, the film is treated as a slightly distorted tetragonal structure for the purposes of lattice parameter determination, since the lattice constants along the direction perpendicular to the films' planes may be slightly different from those along the lateral direction due to the epitaxial mismatch between the FeRhPd and MgO substrate (though the difference is sufficiently small that the impact on the order parameter calculation is negligible). The (001), (002), (101), and (112) lattice spacing values were measured by XRD, and subsequently, those (*hkl*) lattice spacing values were related with the quadratic form of the Bragg equation using a Nelson–Riley extrapolation function to account for systematic errors,

$$\sin^2\theta_i = \frac{\lambda^2}{4a^2}\left(h^2 + k^2 + \frac{a^2}{c^2} l^2\right) + DF(\theta_i), \tag{8}$$

$$F(\theta_i) = \sin^2(2\theta)\left(\frac{1}{\sin\theta} + \frac{1}{\theta}\right), \tag{9}$$

where θ_i are the observed position of the (*hkl*) reflections, a and c the desired lattice parameters, D represents the degree of systematic uncertainty, and $F(\theta)$ is the Nelson–Riley extrapolation function.[22]

TABLE II. Measured I_s/I_f intensity ratio and calculated lattice constants and order parameter S for different growth temperatures T_g and annealing temperatures T_a. The uncertainty in S is taken as ±0.05.

T_g (°C)	T_a (°C)	a (nm)	c (nm)	I_s/I_f	S
400	n/a	0.2974	0.3035	0.831	0.95
500	n/a	0.2993	0.3020	0.820	0.96
600	n/a	0.2996	0.3016	0.720	0.96
700	n/a	0.2996	0.3004	0.811	0.93
400	500	0.2977	0.3040	0.752	0.98
400	600	0.2981	0.3017	0.683	0.93
400	700	0.2992	0.3005	0.755	0.98

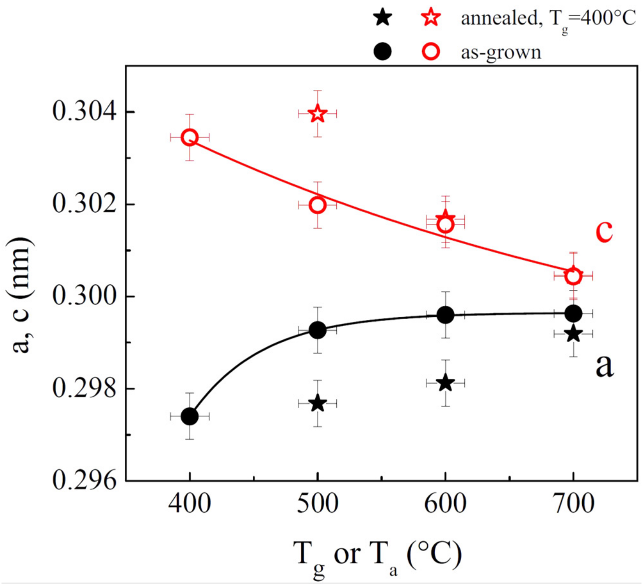

FIG. 5. Values of the lateral (*a*, closed circles) and perpendicular (*c*, open circles) lattice constants for Fe–Rh–Pd films deposited on MgO(001) substrates as a function of the growth temperature. Also shown are samples grown at $T_g = 400\,°C$ and annealed to $T_a = \{500, 600, 700\}\,°C$ (open and closed stars for *c* and *a*, respectively). The uncertainties are smaller than the symbol size; the lines are guides to the eye.

As shown in Fig. 5, the lattice constant along the film normal (*c*) decreased with increasing growth temperature, whereas the lattice constant along the lateral directions (*a*) increased, which can be explained by a lattice mismatch between FeRhPd and MgO. Since MgO has smaller lattice spacing along the lateral directions, it is expected that a compressive stress should result and cause a contraction of the lattice along the lateral (*a*) directions, while the value of the perpendicular lattice constant (*c*) should increase to maintain a constant lattice volume. The compressive strain is relaxed as the growth temperature increases, since the lattice constant values are observed to converge toward their equilibrium values as the growth temperature increases. This change in the crystal structure affects the magnetic transition behavior significantly, even though the degree of chemical order remains essentially constant. The change in the lattice parameters on annealing samples originally grown at T_g to a given temperature T_a is less pronounced than growing the sample at temperature T_a directly, but by 700 °C, one ultimately arrives at essentially the same lattice constants with negligible tetragonal distortion. The same conclusion may be drawn from the FWHM values (not shown), further indicating that while crystalline quality is affected by growth temperature, the order parameter is not substantially influenced. Although the ratio of intensities of the (001) and (002) peaks does not change much; their overall intensity does change. This shows that the film crystallizes in a chemically ordered phase and the fraction of the film that is fully crystallized determines the lattice constant.

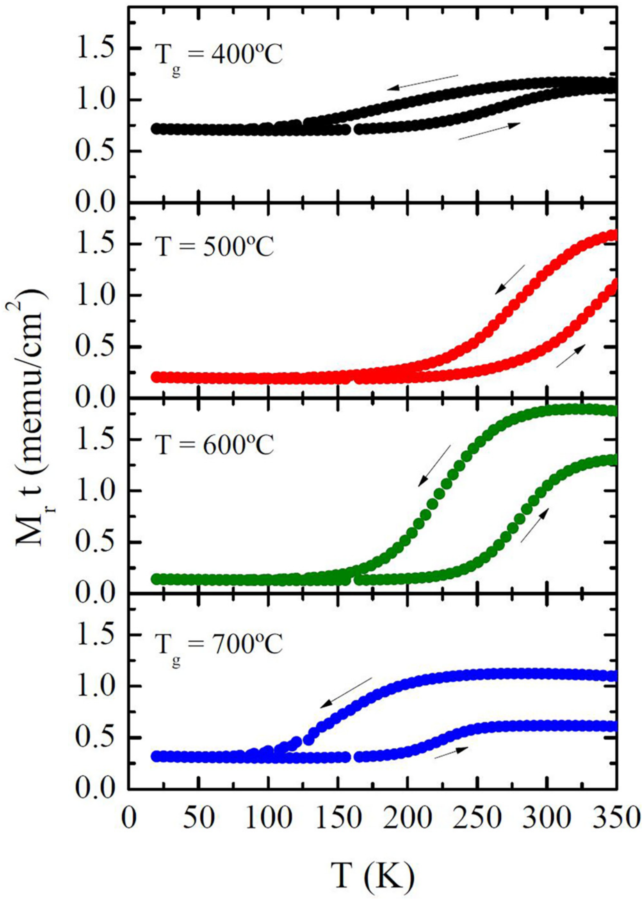

FIG. 6. Remanent magnetization as a function of temperature for as-grown samples with different growth temperatures. No magnetic field was applied during measurement. The offset between the beginning and end of some of the measurements is due to experimental drift.

Figure 6 shows the magnetic transition curves of film grown at different temperatures. No magnetic field was applied during the measurement of the magnetic transition, though the films were magnetically saturated prior to the measurement. The films fabricated from 500 to 700 °C showed an almost complete magnetic transition, whereas the Fe–Rh–Pd film fabricated at 400 °C showed only a partial transition with a large residual ferromagnetic moment even at low temperature. We note that since these measurements are performed in zero applied magnetic field, the transition in warming from the antiferromagnetic state to the ferromagnetic state is necessarily incomplete, as there is no field present to set a preferred magnetization state, resulting in a multidomain state on entering the ferromagnetic phase. This distinct change in the transition temperature with increasing the growth temperature could be a result of the structural change with increasing the growth temperature. If the slight variations in the lattice constants are responsible for the changes in the magnetic ordering temperature, one would expect that the transition for lower T_g

samples should sharpen upon annealing as further relaxation of the epitaxial strain occurs. This is borne out by the results in Fig. 7, where we show the effect of a 30 min anneal at 500 °C or 600 °C on a sample grown at $T_g = 400\,°C$. The incomplete transition for $T_g = 400\,°C$ is now nearly complete, considerably sharper, and at a significantly higher temperature. Most strikingly, compared to an unannealed sample with $T_g = 700\,°C$, the annealed sample shows a much higher transition temperature with a sharper transition. The films grown directly on MgO(100) in this work exhibit different behavior than films grown on buffered α-sapphire at similar growth temperatures,[33] and this emphasizes the sensitivity of the transition temperature to the film structure. The order parameter for all three samples is comparable, which strongly suggests a prominent role of strain relaxation and lattice constant variation in altering the Fe–Fe and Fe–Rh exchange and, in turn, the magnetic phase transition.

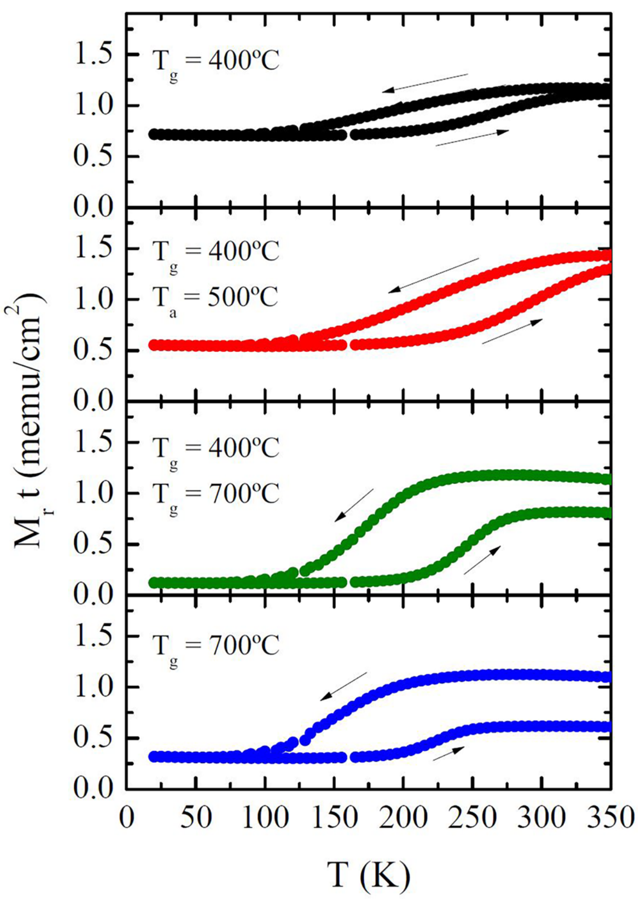

FIG. 7. Remanent magnetization as a function of temperature for as-grown samples with $T_g = 400, 700\,°C$, and samples grown at $T_g = 400\,°C$ and annealed to 500 and 700 °C. A 0.01 T in-plane field was applied during the measurement. The offset between the beginning and end of some of the measurements is due to experimental drift.

TABLE III. Values of the transition temperature and transition width as a function of growth temperatures.

T_g (°C)	T_m (K)	ΔT_m (K)
500	272	72
600	225	90
700	163	104

Returning to Fig. 6, to analyze the transition in more detail, the transition curves were fitted by a linear function near the center of transition (at 50% transition), and the transition temperatures were defined as the temperatures where the slopes in the fitted curves showed maximum values. Transition widths were defined as temperature ranges where the magnetization changed from 90% to 10% of its maximum value, and the extracted values are shown in Table III as a function of the growth temperature. The transition temperature monotonically decreased as the growth temperature increased. This is in sharp contrast to the case of FeRh films on MgO(100), where it was reported that the magnetic transition temperature *increased* as the annealing temperature was increased.[7] The difference between these two experimental results is that our FeRhPd films grown at different temperatures show an increase in *a* and a decrease in *c*, resulting in an almost constant lattice volume (0.8% increase in lattice volume with increasing T_g), whereas for FeRh films,[7] *both a* and *c* decreased as the annealing temperature increased, resulting in a decreased lattice volume.[7] The lattice constants are expected to sensitively impact the magnetic transition as the transition is accompanied by a distinct change in the lattice volume.[9,34,35]

IV. DISCUSSION

A smaller transition slope was also observed in our FeRhPd films compared to other studies.[3–5] This is likely due to residual structural inhomogeneities in thin films as opposed to bulk samples. Since there is some mismatch between the FeRhPd layers and MgO substrates, mismatch strain, plane dislocations, and/or anti phase boundaries are formed. Reducing structural dislocations generally increases the slope of the magnetic transition curve.[36] The transition width (Table III), which is inversely related to the slope of the transition curve, increased with increasing growth temperature. This suggests that structural or compositional inhomogeneities increase with increasing the growth temperature. In this case, it would be most likely that the inhomogeneities are in the lateral directions, since the out-of-plane XRD peaks narrow as growth temperature increases, suggesting less inhomogeneity along the perpendicular direction. This is supported by PEEM observations of a similar film[17] that show mixed phases near the transition temperature. Conversely, a FeRhPd film fabricated at 400 °C and, subsequently, annealed after deposition showed a steeper slope in the transition curve (Fig. 7). Since the annealing treatment should reduce structural inhomogeneities, this result supports our speculation that the changes in the transition temperature and slope result from changes in the lattice parameters, rather than a change in defect concentration or homogeneity. However, given the small Pd content and the small contrast in x-ray scattering factors between Rh and Pd, the degree of ordering within the Rh–Pd sublattice cannot be precisely determined.

Site disorder disrupts long-range magnetic coupling and smears out the Fermi surface. For example, in completely disordered $Ni_{0.8}Fe_{0.2}$, the smearing of the spin-dependent minority band severely shortens the mean free path of these electrons, leading to a reduced magnetic anisotropy and correspondingly low magnetic coercivity.[37] For Fe_2P, which exhibits a first-order magnetic phase transition, off-stoichiometric samples exhibit a significant broadening of the phase transition which is attributed to be of magnetoelastic effects.[38] In more complex alloys such as perskovite manganites, there can be a competition between site-disorder effects and magnetoelastic effects,[39] leading to an ability to tune the phase transition through a wide range of temperatures by using dopants. Recent work has shown that the phase transition behavior of these types of materials is also further modified by size effects.[40–42] Generally speaking, broadening of phase transitions is typically attributed to sample inhomogeneities of disorder. In ultrathin films, a smearing and lowering of the magnetic phase transition occurs when the film thickness approaches the range of spin–spin interactions,[43] which diverge near the phase transition, so it is reasonable to expect that films with grain sizes on the order of a few nanometers may exhibit a broadening and/or lowering of the phase transition temperature.

The nucleation process during the transition phase likely has an electronic origin stemming from the competition[15] between antiferromagnetic Fe–Fe exchange coupling (J_{Fe-Fe}) and ferromagnetic coupling mediated by Rh magnetic moments which are induced by thermal fluctuations ($J_{Fe-Rh-Fe}$). We propose that the transition temperature variation (e.g., with deposition conditions) originates from the variation of exchange coupling constants with lattice spacing, thus revealing fundamental information on the nature of magnetic interactions in these alloys. The electronic origin of the phase transition is further suggested by a comparison of the resistivity and magnetic moment as a function of temperature.[12,44,45] Figure 8 shows the inverse resistance R^{-1} (measured in an applied field of 0.01 T) and magnetic moment (measured in zero magnetic field) as a function of temperature for a sample grown at $T_g = 470\,^\circ$C. Plotting $R^{-1}(T)$ rather than $R(T)$ is simply to make more readily apparent the close relationship between magnetic moment and conductivity. Both the resistance and magnetic moment exhibit a hysteretic transitions as a function of temperature, with a clear increase of the resistivity as FeRhPd enters the antiferromagnetic phase, consistent with previous work.[45,46] In all samples investigated over a full thermal cycle, a hysteretic transition was observed, in both magnetic moment and resistance. This is also evidenced in Fig. 8, where a sample grown at $T_g = 400\,^\circ$C and annealed to 700 °C displays a much larger and sharper resistive and magnetic transition, with a correspondingly smaller hysteresis in the transition. The magnetic transition is essentially complete, and the resistance changes by nearly 60%. We note that the resistance measurements were performed on sheet films using a four-point van der Pauw technique,[47,48] so we are necessarily insensitive to any in-plane anisotropy of the resistivity.

Previous investigations,[12,44–46,49] both experimental and theoretical, have attributed the large increase in resistivity upon

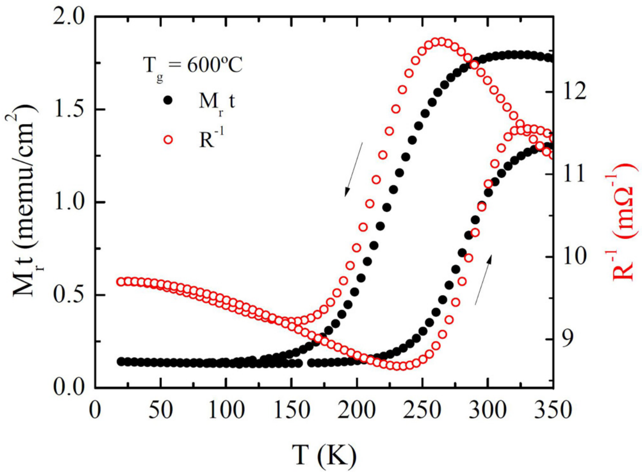

FIG. 8. Magnetic moment (closed) and inverse resistance R^{-1} (open) vs temperature for a sample grown at $T_g = 600\,^\circ$C, both exhibiting hysteretic transitions. The resistance was measured with the zero applied field, and the magnetic moment with a 0.01 T in-plane magnetic field. The offset between the beginning and end of the magnetic moment measurement is due to experimental drift.

entering the antiferromagnetic state to the layered antiferromagnetic structure, leading to a spin-dependent scattering analogous to giant magnetoresistance.[12,44,49] The resistive transition should originate from spin-dependent scattering, since phonon and impurity contributions do not change significantly across the transition, and no structural transition occurs.[45] In the antiferromagnetic state, the lowest energy configuration of FeRh is a type II antiferromagnet, with (100) iron layers with alternating spins within the planes, and rhodium layers with zero spin between[12] a unit-cell-level analog of an antiferromagnetically coupled magnetic multilayer. Additional scattering due to Pd impurities or substitutional disorder serves to increase the spin-dependent scattering and further increase the resistance of the antiferromagnetic state.[50] In the ferromagnetic state, all Fe moments are aligned, and a Rh local moment is induced, aligned nominally parallel to Fe but thermally fluctuating. Thus, in the antiferromagnetic state, we expect an increased resistance due to the spin-dependent scattering by alternating Fe spins, while in the ferromagnetic phase, this additional resistance contribution is absent, and the overall resistivity should be more strongly temperature-dependent in the ferromagnetic state due to spin scattering by the thermally fluctuating Rh moment. This qualitatively explains our observations that resistivity increases on entering the antiferromagnetic state, resistance and magnetic moment are closely linked, and the ferromagnetic state has a stronger temperature dependence of the resistance, and together they strongly suggest a common electronic origin for both the resistive and magnetic transition. Though in principle both mechanisms should give rise to characteristic temperature dependencies,[45] $R \sim T^2$ in the ferromagnetic state and $R \sim T$ in the antiferromagnetic state, the present data appear to scale equally well with T, T^2, or T^{-1} in both regimes, probably owing to the limited temperature ranges investigated; more extensive studies are under way.

V. THEORETICAL RESULTS

In order to rationalize the observed trend in the transition temperature T_m with growth temperature T_g and lattice constants, we used a classical isotropic effective spin model,

$$H = -\sum_{i \neq j} J_{ij}\vec{S}_i\vec{S}_j - \sum_{\nu} I m_{\nu}^2. \tag{10}$$

Here, the first term represents Heisenberg exchange for Fe and the second term represents Stoner interactions for Fe ($\vec{S}$) and Rh (m_{Rh}) spin degrees of freedom.[15,51–53] The first term physically represents the exchange energy due to Fe–Fe spin moment (antiferromagnetic) interactions, for which we use notation $J_{\mathrm{Fe-Fe}}$, while the second term can be viewed as a temperature-dependent exchange interaction between Fe atoms mediated by the induced Rh moments m_ν, for which we use notation $J_{\mathrm{Fe-Rh-Fe}}$. The latter is effectively a ferromagnetic exchange interaction and is very strong due to large Rh Stoner parameter I.[15,53] The competition of the antiferromagnetic $J_{\mathrm{Fe-Fe}}$ interactions and strongly temperature dependent ferromagnetic $J_{\mathrm{Fe-Rh-Fe}}$ interactions leads to a nucleation of the ferromagnetic (in heating) or ferromagnetic (in cooling) phase in FeRh at characteristic temperature T_m. The observed change in lattice parameters (a and c) on deposition temperature T_g has only a very small effect on the $J_{\mathrm{Fe-Rh-Fe}}$ interactions. This conclusion follows from direct calculations[15] and seems reasonable since the intra-atomic exchange parameter [second term in Eq. (10)] is generally much less sensitive to environment than interatomic exchange. In this light, for understanding the observed change in T_m with lattice spacing, it is sufficient to focus on how the antiferromagnetic $J_{\mathrm{Fe-Fe}}$ interactions depend on the lattice parameters within the observed range.

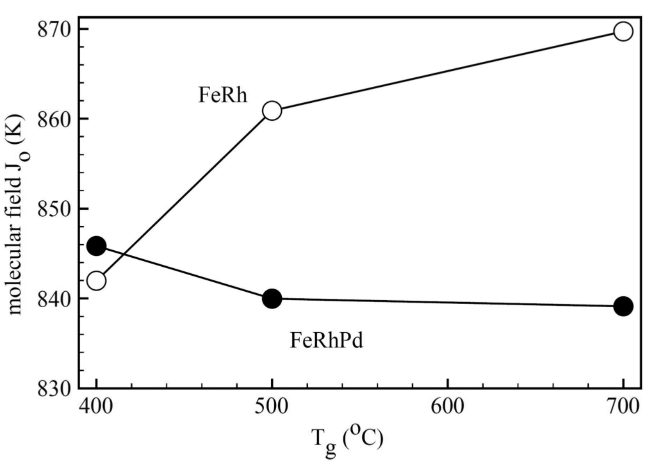

FIG. 9. Calculated parametric dependence of molecular field or antiferromagnetic order stability parameter J_0 (K) on $a(T_g)$, $c(T_g)$.

We performed constrained density functional calculations for noncollinear spin configurations in order to quantify the dependence of $J_{\mathrm{Fe-Fe}}$ on lattice parameters[54–56] and for infinitesimal angle perturbations[57] to determine the molecular field parameter (or antiferromagnetic order stability parameter) J_0. These two approaches are implemented using the linearized muffin-tin orbital method within the atomic sphere approximation (LMTO-ASA),[58,59] performed for the type II antiferromagnetic ground state of B2 FeRh. We find that both methods give very similar results in terms of the calculated J_0 values. Since within the approximations noted above the critical temperature (nucleation temperature) variation is proportional to the antiferromagnetic order stability parameter, the dependence of J_0 on lattice parameters should give an estimate of the transition temperature T_m trend with growth temperature T_g via the measured dependence of the lattice constants a and c on growth temperature.

In Fig. 9, we show the parametric dependence of J_0 on T_g calculated both for the FeRhPd films measured in this work and for pure FeRh,[7] using the experimentally determined lattice constants in the calculations in order to relate J_0 to T_g. We find that our proposed model explains the observed trend in both cases. Most notably, the nucleation/transition temperature *increases* for Fe–Rh and *decreases* for Fe–Rh–Pd alloys as T_g increases, in agreement with Ref. 7 and our measurements. This suggests that variation of lattice parameters driven by growth temperature T_g variations alters primarily the strength of the antiferromagnetic $J_{\mathrm{Fe-Fe}}$ interactions. As a result, our study of the growth temperature and lattice constant dependence of the magnetic transition effectively enables us to probe Fe–Fe exchange interactions and their dependence on lattice parameters.

Based on our observations and supported by our calculations, small Pd additions to FeRh lead to a fundamental difference of the dependence of T_m on processing. The change of lattice constants with high temperature growth or annealing is altered with Pd doping and this modifies the phase transition behavior. Importantly, from a technological point of view the transition temperature and transition width can be readily tuned by simply altering fabrication conditions. For example, the transition temperature of Fe–Rh in heat assisted magnetic recording media should be optimized so that the dynamic coercivity of the media at the highest temperature can be suppressed well below the limited writing field available. Further tuning of the strain may be accomplished by using appropriate seed or buffer layers during fabrication. Changing the amount of dopant is an effective way to change the transition temperature, while optimizing the processing conditions provides an effective means to tune both the transition temperature and the width of the transition. The computed link between the lattice constant and exchange constant provides a way to predict the outcome based on the structural changes.

VI. CONCLUSIONS

In summary, epitaxial ternary alloy $Fe_{47}Rh_{47}Pd_6$ films were fabricated on MgO(001) substrates. The films exhibit a reduction in the transition temperature with an increase in the growth temperature, which can be attributed to changes in the lattice parameters.

These results show an opposite tendency compared to Fe–Rh binary alloy films. This tendency is attributed to how the lattice parameters change under different processing conditions. Significant property variations may be achieved through high temperature deposition as compared to postdeposition annealing.

ACKNOWLEDGMENTS

The authors gratefully acknowledge financial support from DOE Award No. DE-FG02-08ER46499. The theoretical calculations in this work were performed by Oleg Mryasov, who is deceased. The authors hope that this work is contributed to his legacy. His legacy lives on in this paper and in our respect for him.

DATA AVAILABILITY

The data that support the findings of this study are available from the corresponding author upon reasonable request.

REFERENCES

[1] M. Fallot, Ann. Phys. **11**, 291 (1938).
[2] M. Fallot and R. Hocart, Rev. Sci. **77**, 498 (1939).
[3] N. V. Baranov and E. A. Barabanova, J. Alloys Compd. **219**, 139 (1995).
[4] J. S. Kouvel, J. Appl. Phys. **37**, 1257 (1966).
[5] P. H. L. Walter, J. Appl. Phys. **35**, 938 (1964).
[6] P. Kushwaha, A. Lakhani, R. Rawat, and P. Chaddah, Phys. Rev. B **80**, 174413 (2009).
[7] J. Cao, N. T. Nam, S. Inoue, H. Y. Y. Ko, N. N. Phuoc, and T. Suzuki, J. Appl. Phys. **103**, 07F501 (2008).
[8] M. Jiang, X. Z. Chen, X. J. Zhou, Y. Y. Wang, F. Pan, and C. Song, J. Cryst. Growth **438**, 19 (2016).
[9] J.-U. Thiele, S. Maat, J. L. Robertson, and E. E. Fullerton, IEEE Trans. Magn. **40**, 2537 (2004).
[10] J.-U. Thiele, S. Maat, and E. E. Fullerton, Appl. Phys. Lett. **82**, 2859 (2003).
[11] K. Y. Guslienko, O. Chubykalo-Fesenko, O. Mryasov, R. Chantrell, and D. Weller, Phys. Rev. B **70**, 104405 (2004).
[12] V. L. Moruzzi and P. M. Marcus, Phys. Rev. B **46**, 14198 (1992).
[13] K. A. Gschneidner, Jr., V. Pecharsky, and A. Tsokol, Rep. Prog. Phys. **68**, 1479 (2005).
[14] M.-H. Phan and S.-C. Yu, J. Magn. Magn. Mater. **308**, 325 (2007).
[15] G. Ju, J. Hohlfeld, B. Bergman, R. J. van de Veerdonk, O. N. Mryasov, J.-Y. Kim, X. Wu, D. Weller, and B. Koopmans, Phys. Rev. Lett. **93**, 197403 (2004).
[16] S. Maat, J.-U. Thiele, and E. E. Fullerton, Phys. Rev. B **72**, 214432 (2005).
[17] C. J. Kinane *et al.*, New J. Phys. **16**, 113073 (2014).
[18] C. Baldasseroni *et al.*, J. Appl. Phys. **115**, 043919 (2014).
[19] B. Cordero, V. Gómez, A. E. Platero-Prats, M. Revés, J. Echeverría, E. Cremades, F. Barragán, and S. Alvarez, Dalton Trans. **21**, 2832 (2008); available at https://pubs.rsc.org/en/content/articlelanding/2008/dt/b801115j.
[20] B. E. Warren, *X-Ray Diffraction* (Addison Wesley, Reading, MA, 1969).
[21] D. Lott, J. Fenske, A. Schreyer, P. Mani, G. Mankey, F. Klose, W. Schmidt, K. Schmalzl, and E. Tartakovskaya, Phys. Rev. B **78**, 174413 (2008).
[22] B. D. Cullity and S. R. Stock, *Elements of X-Ray Diffraction* (Prentice Hall, Upper Saddle River, NJ, 2001), p. 388.
[23] H. Xiao and I. Baker, Acta Metall. Mater. **42**, 1535 (1994).
[24] H. Xiao and I. Baker, Acta Metall. Mater. **43**, 391 (1995).
[25] S. Okamoto, O. Kitakami, and Y. Shimada, J. Magn. Magn. Mater. **208**, 102 (2000).
[26] Z. Lu , M. J. Walock, P. R. LeClair, and G. J. Mankey, J. Vac. Sci. Technol. A **27**, 770 (2009).
[27] L.-M. Peng, G. Ren, S. Dudarev, and M. Whelan, Acta Cryst. **A52**, 456 (1996).
[28] C. T. Chantler, J. Phys. Chem. Ref. Data **24**, 71 (1995).
[29] C. T. Chantler, J. Phys. Chem. Ref. Data **29**, 597 (2000).
[30] J. K. Baria, Czech. J. Phys. **54**, 575 (2004).
[31] M. Cohen, Rev. Sci. Instrum. **6**, 68 (1935).
[32] M. Cohen, Rev. Sci. Instrum. **7**, 155 (1936).
[33] J. H. Lee, Y. C. Shin, S.-M. Lee, O. S. Jin, S. H. Kang, S. W. Hong, C.-M. Jeong, J. B. Huh, and D.-W. Han, Sci. Rep. **5**, 18833 (2015).
[34] A. Zakharov, A. M. Kadomtseva, R. Z. Levitin, and E. G. Ponyatovskii, Zh. Eksp. Teor. Fiz. **46**, 2003 (1964).
[35] L. Zsoldos, Phys. Status Solidi B **20**, K25 (1967).
[36] P. Kushwaha, A. Lakhani, R. Rawat, and P. Chaddah, Phys. Rev. B **80**, 174413 (2009).
[37] D. Y. Petrovykh, K. N. Altmann, H. Höchst, M. Laubscher, S. Maat, G. J. Mankey, and F. J. Himpsel, Appl. Phys. Lett. **73**, 3459 (1998).
[38] L. Lundgren, G. Tarmohamed, O. Beckman, B. Carlsson, and S. Rundqvist, Phys. Scr. **17**, 39 (1978).
[39] Q. Ji, B. Lv, Q. Xie, R. Xie, Z. Jiang, F. Zhang, and X. Wu, IEEE Trans. Magn. **47**, 2466 (2011).
[40] S. S. Rao, K. N. Anuradha, S. Sarangi, and S. V. Bhat, Appl. Phys. Lett. **87**, 182503 (2005).
[41] H. Das, G. Sangiovanni, A. Valli, K. Held, and T. Saha-Dasgupta, Phys. Rev. Lett. **107**, 197202 (2011).
[42] T. Zhang and M. Dressel, Phys. Rev. B **80**, 014435 (2009).
[43] R. Zhang and R. F. Willis, Phys. Rev. Lett. **86**, 2665 (2001).
[44] N. V. Baranov, P. E. Markin, S. V. Zemlyanski, H. Michor, and G. Hilscher, J. Magn. Magn. Mater. **157**, 401 (1996).
[45] S. Yuasa, T. Akiyama, H. Miyajima, and Y. Otani, J. Phys. Soc. Jpn. **64**, 3978 (1995).
[46] J. M. Lommel, J. Appl. Phys. **37**, 1483 (1966).
[47] L. J. Van der Pauw, Philips Res. Rep. **13**, 1 (1958).
[48] L. J. Van der Pauw, Philips Tech. Rev. **20**, 220 (1958).
[49] V. Schovsky, L. Havela, K. Prokes, H. Nakotte, F. R. de Boer, and E. Bruck, J. Appl. Phys. **76**, 6913 (1994).
[50] I. Turek, J. Kudrnovskỳ, V. Drchal, P. Weinberger, and P. H. Dederichs, Czech. J. Phys. **52**, 203 (2002).
[51] O. N. Mryasov, U. Nowak, K. Y. Guslienko, and R. W. Chantrell, Europhys. Lett. **69**, 805 (2005).
[52] O. N. Mryasov, J. Magn. Magn. Mater. **272**, 800 (2004).
[53] O. N. Mryasov, Phase Trans. **78**, 197 (2005).
[54] O. N. Mryasov, V. A. Gubanov, and A. I. Liechtenstein, Phys. Rev. B **45**, 12330 (1992).
[55] O. N. Mryasov, R. F. Sabiryanov, A. J. Freeman, and S. S. Jaswal, Phys. Rev. B **56**, 7255 (1997).
[56] O. N. Mryasov, A. I. Liechtenstein, L. M. Sandratskii, and V. A. Gubanov, J. Phys.: Condens. Matter **3**, 7683 (1991).
[57] V. Heine, A. I. Liechtenstein, and O. N. Mryasov, Europhys. Lett. **12**, 545 (1990).
[58] O. K. Andersen, O. Jepsen, and M. Sob, “Linearized band structure methods,” in *Electronic Band Structure and Its Applications* (Springer, Berlin, 1985), pp. 1–57.
[59] M. V. Shilfgaarde and W. R. L. Lambrecht, “Tight-binding linear muffin-tin orbital implementation of the difference equation Green’s function approach for 2D-periodic systems,” in *MRS Online Proceedings Library (OPL)* 491 (Cambridge University, Cambridge, 1998).